Organic & Biomolecular Chemistry

Accepted Manuscript

This article can be cited before page numbers have been issued, to do this please use: T. Milcent, M. L. Gelmi, J. Kaffy, B. Crousse, M. Saraç, R. R.BR. Brandt, B. Gigant, F. Giraud, V. Campanacci, K. Peqini, C. Vanoni, S. Ongeri, L. Singh and A. Wetjen, *Org. Biomol. Chem.*, 2026, DOI: 10.1039/D6OB00187D.

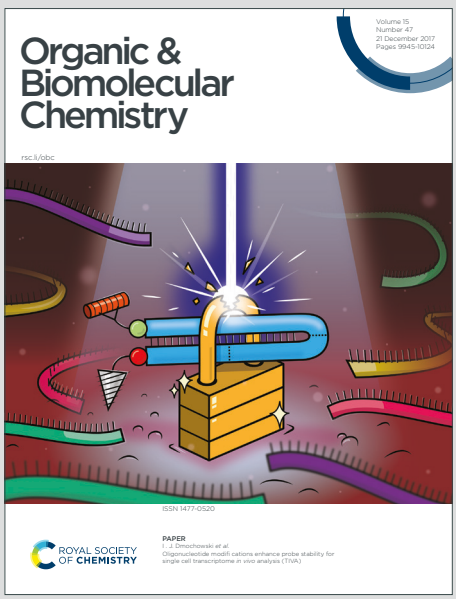

ROYAL SOCIETY OF CHEMISTRY

rsc.li/obc

View Article Online
DOI: 10.1039/D6OB00187D

ARTICLE

A β-hairpin mimic built on a fluorinated isoxazoline-β^{2,2}-amino acid as a modulator of Tau protein aggregation

Received 00th January 20xx,
Accepted 00th January 20xx

DOI: 10.1039/x0xx00000x

Murat Saraç,[a] Julia Kaffy,[a] Kaliroi Peqini,[b] Caterina Vanoni,[a,b] Alina Wetjen,[c] Lisha Singh,[c] Roland Brandt,[c] Valérie Campanacci,[d] Benoît Gigant,[d] François Giraud,[e] Benoît Crousse,[a] Sandrine Ongeri,[a] Maria Luisa Gelmi,*[b] Thierry Milcent*[a].

Alzheimer's disease (AD), the leading cause of dementia, is a tauopathy characterized by the intraneuronal accumulation of misfolded Tau into neurofibrillary tangles that drive synaptic dysfunction and neuronal loss. Molecular chaperones such as Hsp90 regulate Tau folding, degradation, and aggregation, but full-length chaperones are not viable drugs, prompting the development of peptidomimetics that reproduce protective Hsp90–Tau contacts. We previously reported two β-hairpin peptidomimetics derived from Hsp90, based on a piperidine-pyrrolidine (β-HM1) or on an isoxazoline amino acid (β-HM2) incorporating key hot-spot sequences, that inhibit the aggregation of wild-type and ΔK280 Tau and restore Tau–microtubule interactions in cells. Here, we describe the design and characterization of fluorinated β-HM2 analogues (β-FH1 and β-FH2) as molecular tools to investigate the mechanism of Tau misfolding. β-FH1 and β-FH2 contain a fluorinated isoxazoline-β^{2,2}-amino acid scaffold whose *S* or *R* stereochemistry biases the peptidomimetic toward either a fully extended β-strand-like conformation or a β-hairpin fold, respectively. The replacement of the phenyl group of the Isox-β^{2,2}-AA core by a trifluoromethyl substituent was intended to refine Tau anti-aggregation activity, enhance metabolic stability toward proteolysis, and introduce a sensitive ^{19}F NMR probe to monitor Tau–peptidomimetic interactions at the molecular level. The fluorinated analogues completely lost their ability to prevent tau aggregation in model neurons but caused increased dynamics of the Tau-microtubule interaction. This suggests that subtle changes in β-hairpin preorganization and flexibility impair optimal Tau recognition and affect Tau function in neuronal cell processes. This underlines the need for finely tuned hairpin architectures in the design of chaperone-mimetic peptides.

Introduction

Alzheimer's disease (AD), the leading cause of dementia, is a neurodegenerative disorder whose incidence increases with age and constitutes a substantial burden for healthcare systems.[1] Current pharmacological options provide, at best, modest and transient benefit, are often limited by adverse effects, and have not demonstrated sustained disease modification, underscoring the urgent need for safer and more effective therapies. AD is characterized by the formation of Aβ$_{1\text{-}42}$ and Tau protein aggregates. Despite ongoing debate regarding their clinical meaningfulness and their substantial costs, three anti-Aβ$_{1\text{-}42}$ monoclonal antibodies have recently reached clinical practice through regulatory pathways. Aducanumab (approved by the FDA in June 2021),[2] Lecanemab (approved by the FDA in July 2023 and by the EMA in November 2024),[3–6] and Donanemab (approved by the FDA in July 2024).[7–9] However, to date, no drug targeting Tau has been approved for the therapeutic treatment of AD.

The physiological role of Tau, one of the microtubule-associated proteins (MAPs), appears to regulate the polymerization of axonal microtubules (MTs) to support axonal transport and neuronal plasticity.[10] Under pathological conditions, conformational changes of Tau and its detachment from microtubules occur, and the accumulation of misfolded Tau protein aggregates forming soluble oligomers, paired helical filaments (PHFs) and intracellular neurofibrillary tangles (NFTs)[11] cause the neuronal dysfunction and cell death in Tauopathies, such as AD.[12] An abnormal hyperphosphorylation of Tau is also observed in AD, however the effect of Tau phosphorylation on fibrilization and aggregation is still unclear and highly debated.[13] The management of the misfolded proteins levels in healthy neurons depends on the chaperone protein families. In addition to their role in the folding of polypeptides synthesized by ribosomes, they recognize misfolded proteins and facilitate their folding or degradation, thus preventing their pathological aggregation.[14–16] As we age, their function declines, leading to misfolded proteins

[a] Université Paris-Saclay, CNRS, BioCIS, Bat. Henri Moissan, 17 av. des Sciences, 91400 Orsay, France. Email : thierry.milcent@universite-paris-saclay.fr
[b] Dipartimento di Scienze Farmaceutiche, DISFARM, Università degli Studi di Milano, Via Venezian 21, Milano, 20133, Italy. Email: marialuisa.gelmi@unimi.it
[c] Department of Neurobiology, Osnabrück University, Barbarastrasse 11, 49076 Osnabrück, Germany.
[d] Université Paris-Saclay, CEA, Institute for Integrative Biology of the Cell (I2BC), 91198 Gif-sur-Yvette, France CNRS, Paris, France.
[e] Laboratoire de RMN Biologie et Chimie Structurales, CNRS, Institut de Chimie des Substances Naturelles, 1, av. de la Terrasse, 91190 Gif-sur-Yvette, France.
† Footnotes relating to the title and/or authors should appear here.
Supplementary Information available: [details of any supplementary information available should be included here]. See DOI: 10.1039/x0xx00000x

View Article Online
DOI: 10.1039/D5OB00187D

accumulating and aggregating.[17,18] Although the molecular mechanism by which these chaperones maintain the healthiness of neurons remains unclear, it has been shown that the Tau protein interacts with members of these canonical families.[19–21]

Among these chaperones, Hsp90's whose role in neurodegeneration and interaction with Tau are controversial, is suggested to favor the formation of less toxic Tau aggregates, and the formation of Hsp90-Tau complexes might prevent harmful interactions with cytoplasmic proteins.[22–30] However, the effect of Hsp90 on Tau's physiological interaction with microtubules is still unclear. As full-length chaperone proteins are not viable drugs due to pharmacokinetic and cost issues, we recently proposed the use of small peptidomimetics based on Hsp90-Tau interactions to mimic Hsp90 chaperone activity.[31,32] Peptides are preferred over small molecules for targeting protein-protein interactions (PPIs) because they can mimic and modulate flexible hot-spot regions and offer greater affinity, selectivity, and safety.[33–36] However, their proteolytic instability and inability to form stable structures are challenges.[35,37] Therefore, the incorporation of non-natural amino acids helps stabilize these peptides towards proteolysis and promotes bioactive conformations.[37,38] In order to mimic the Hsp90-Tau interaction and to explore its role in Tau misfolding and aggregation, we recently reported two Hsp90 chaperone-inspired peptidomimetics designed to potentially reduce Tau fibrillization and clarify Hsp90's influence on Tau's microtubules interaction.[31,32] Key sequences of Hsp90 interacting with Tau were identified using results from Small-Angle X-ray Scattering (SAXS) and Nuclear Magnetic Resonance (NMR) experiments.[39] While exact interacting residues remain unknown, the crystal structure of Hsp90's *N*-terminal domain (^{N}Hsp90; PDB = 3NMQ) helped pinpoint relevant regions and hotspots.[40] Four sequences were identified as crucial for interaction, with S4 (residues 144-152) and S7 (residues 181-189) being particularly important. Recently, two β-hairpin mimic peptides **β-HM1** (corresponding to **β-Hsp90** in ref. 31)[31] and **β-HM2** (corresponding to compound **3** in ref. 32)[32], based on 1-[(3*R*,4*R*)4-tosylamidopiperidin-3-yl]pyrrolidine-2-carboxylic acid (piperidine –pyrrolidine scaffold) or 5-(aminomethyl)-3-phenyl-4,5-dihydroisoxazole-5-carboxylic acid (Isoxazoline-β^{2,2}-amino acid, *i.e.* Isox-β^{2,2}-AA), respectively, as β-turn inducers, and short S4 and S7 hexapeptidic sequences (^{146}KVVVIT^{151} and ^{183}TKVILH^{188}, core sequences of S4 and S7, respectively), were selected to optimize interaction with Tau (**Fig. 1**).

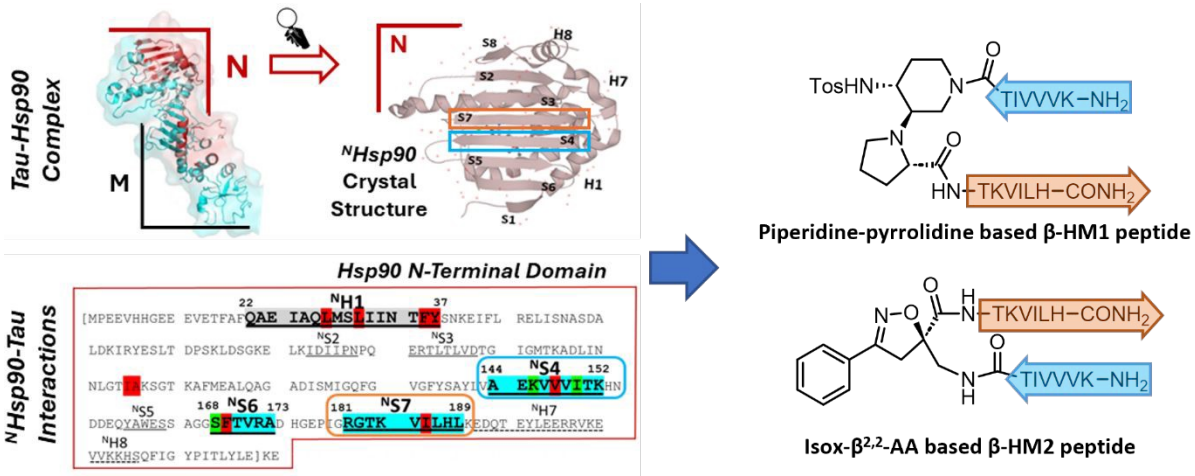

Fig. 1. Structural representation of the crystal structure of the Hsp90-Tau complex;[40] mapped interaction sequences between Hsp90 and Tau (only Hsp90 residues are represented),[39] and structures of **β-HM1**[31] and **β-HM2**[32] peptidomimetics.

These two peptidomimetics, incorporating key Hsp90 sequences, effectively inhibited Tau aggregation, including both wild-type Tau (Wt-Tau441)[31,32] and the pro-aggregative Tau-ΔK280 mutant,[31] as shown by Thioflavin-T (ThT) fluorescence spectroscopy. Transmission electron microscopy (TEM) revealed the dramatic perturbation of the morphology of Tau species in the presence of **β-HM1** with the stabilization of intermediate structures and the inhibition of mature amyloid fibrils. Live cell imaging FDAP (fluorescence decay after photoactivation) confirmed that **β-HM1** prevented Tau aggregation and restored Tau-microtubule (MT) interaction in model neurons to normal levels. The interaction of **β-HM1** with Tau's P1 region was validated through ^{15}N-HSQC titrations. Additionally, **β-HM1** also acted as a dual inhibitor of both Tau and A$\beta_{1\text{-}42}$ aggregation, as shown by ThT and TEM experiments.[31]

Taking all these considerations into account, we present here the design, synthesis, and evaluation of a new fluorinated analogue of **β-HM2** peptidomimetic as a molecular tool to investigate the mechanism of inhibition of Tau aggregation by small synthetic chaperone inspired by Hsp90. Fluorine substituents are commonly used in the pharmaceutical industry, with about 20% of drugs on the market containing at least one fluorine atom. Fluorine is often added to bioactive molecules in order to improve their physicochemical properties and ADME (absorption, distribution, metabolism, and excretion) characteristics.[41–44] Beyond small molecules, fluorine has emerged as a valuable tool to fine-tune the structural and biophysical properties of peptides and proteins.[45–51] Introduction of fluorinated substituents can modulate side-chain interactions, stabilize or bias secondary structure elements, and alter local folding landscapes due to the strong inductive effects and unique steric profile of fluorine-

View Article Online DOI: 10.1039/D5OB01870D

containing groups such as trifluoromethyl. Importantly, fluorination may increase proteolytic stability by reducing susceptibility to enzymatic cleavage, a critical parameter for peptide-based therapeutics. In addition to these physicochemical and pharmacokinetic advantages, fluorine offers exceptional spectroscopic benefits. The ^{19}F nucleus combines 100% natural abundance, high sensitivity, and absence in most biological backgrounds, making ^{19}F-NMR a uniquely powerful, non-invasive probe to monitor molecular recognition events with high selectivity and minimal signal overlap. Consequently, the introduction of fluorine atoms into proteins or peptides enables investigating biological processes with ^{19}F-NMR spectroscopy, providing a better understanding of the structure and function of biomolecules, especially ligand-biomolecule interactions.[52–56] Based on these advantages, we replaced the phenyl group of the isoxazoline core in **β-HM2** peptidomimetic with a trifluoromethyl substituent (peptidomimetic **β-FH2**), in order to evaluate the ability of the fluorinated moiety to improve the activity and/or the metabolic stability towards proteolysis and to serve as a ^{19}F-NMR probe enabling us to explore the molecular-level interaction between Tau protein and our peptidomimetic (**Fig. 2**). Surprisingly, the trifluoromethyl substituent compromised the β-hairpin conformation of **β-FH2** and attenuated its inhibitory activity against Tau aggregation, underscoring the importance of β-hairpin integrity for effective Hsp90-mimic function.

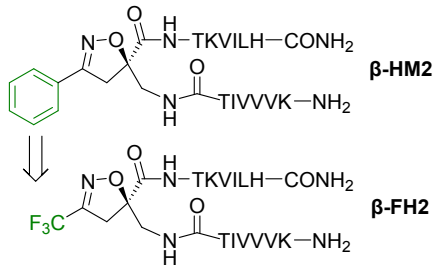

Fig. 2. Fluorinated analogue of **β-HM2** peptidomimetic: **β-FH2**.

Results and discussion

Design

The design of peptidomimetic **β-FH2** was based on our earlier findings showing that the β-hairpin mimic **β-HM2**, containing specific sequences (cores of S4 and S7) from the *N*-terminal region of Hsp90, can inhibit aggregation of both Wt-Tau441 and Tau-ΔK280 mutant.[32] This **β-HM2** peptidomimetic was designed from the non-coded isoxazoline-$\beta^{2,2}$-substituted amino acid (Isox-$\beta^{2,2}$-AA) core, which can promote β-turn like or extended conformation when incorporated into peptide sequences depending on the absolute *R*- or *S*- configuration at the isoxazoline C-5 position.[57] Building on these findings, we based our design on the trifluoromethyl analogue of Isox-$\beta^{2,2}$-AA and the specific sequences (cores of S4 and S7) from the *N*-terminal region of Hsp90.

To distinguish how peptide conformation affects Hsp90 mimic-Tau interaction, the stereochemical tool Isox-$\beta^{2,2}$-AA was used to bias peptidomimetics **β-FH1** and **β-FH2** toward distinct structural states. According to our previous finding, the *S*-configuration should stabilize an extended β-strand–like conformation and should not impact Tau aggregation, whereas the *R*-configuration should favor a β-hairpin–like fold and thus inhibit Tau aggregation (**Fig. 3**).

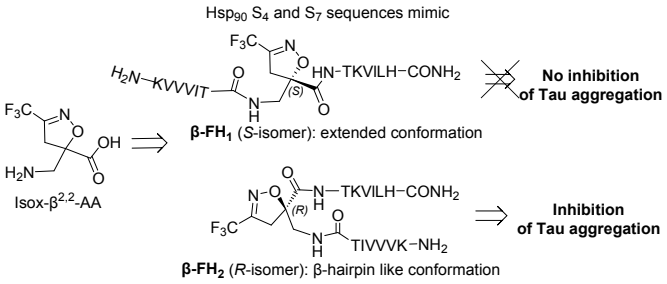

Fig. 3. Design of peptidomimetics **β-FH1** and **β-FH2**: expected conformation and activity on Tau aggregation

Synthesis

The key step of the synthesis of the trifluoromethyl isoxazoline scaffold is the [3+2] cycloaddition reaction between the azido-derivative of the methyl 2-(azidomethyl)acrylate and the nitrile oxide **1c** generated from the corresponding trifluoroacetaldehyde oxime **1**. According to the previously described procedure, the oxime **1** was prepared from the commercially available trifluoroacetaldehyde hydrate and an aqueous solution of hydroxylamine (50 wt.%).[57] After stirring at room temperature for 18 hours, the resulting aldoxime **1** was purified by fractional distillation (b.p. 80°C), affording the product in 62% yield. Then the aldoxime **1** was subsequently converted into the corresponding chloro-oxime **1b** using *N*-chlorosuccinimide (NCS) in chloroform, catalysed by one drop of trimethylchlorosilane. Owing to its high instability, the chloro-oxime **1b** was not isolated and was directly engaged in the next step. The nitrile oxide **1c** was generated *in situ* upon adding $NaHCO_3$ and reacted overnight with the azido methacrylate via a 1,3-dipolar cycloaddition affording the corresponding isoxazoline **2** in 45% yield (**Scheme 1**).

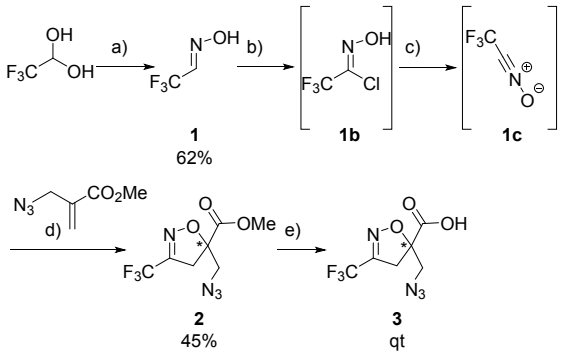

Scheme 1. Synthesis of CF_3-Isox-$\beta^{2,2}$-azido acid 3. a) NH_2OH 50% wt. in water, 18 h, rt. **b)** *N*-chlorosuccinimide (1.3 eq.), trimethylchlorosilane (1 drop), $CHCl_3$, 18 h, rt. **c)** $NaHCO_3$ (1.5 eq.), 1 min, rt. **d)** methyl 2-(azidomethyl)acrylate (1.1 eq.), 18 h, rt. **e)** $LiOH_{aq}$ (1.5 eq., 0.1 M), THF/H_2O, 30 min, rt.

View Article Online
DOI: 10.1039/D6OB00187D

As expected, and in line with previous reports, the 1,3-dipolar cycloaddition proceeded with complete regioselectivity to afford exclusively the C5-disubstituted isoxazoline product **2** in racemic form. The corresponding carboxylic acid **3** was then obtained quantitatively by saponification of the methyl ester (LiOH, THF/H_2O). **β-FH1** and **β-FH2** were then directly and fully synthesized on solid-phase according to **Scheme 2**. Couplings of the first six commercially available Fmoc-protected amino acids were performed at room temperature using HCTU in DMF containing 20% NMM, with Fmoc removal carried out under standard conditions (20% piperidine in DMF). After that, the coupling of the racemic mixture of CF_3-Isox-$\beta^{2,2}$-azido acid **3** (2 eq.) was carried out in DMF, oxyma (2 eq.) and DIC (2 eq.). Before continuing the peptide elongation, the azido moiety was reduced ($N_3 \rightarrow NH_2$) on resin via a Staudinger reaction, using trimethylphosphine (7 eq.) in toluene in the presence of H_2O (49 eq.) at room temperature. Subsequent amino acid couplings were carried out under the same conditions as before (oxyma/DIC/DMF), and the diastereoisomeric peptidomimetics were cleaved from the resin under acidic conditions (TFA/H_2O/TIPS/Phenol, 90/5/2.5/2.5). In contrast, the synthesis of **β-HM2** required a preliminary solution-phase assembly of the Fmoc-Phe-Isox-$\beta^{2,2}$-Thr(OtBu)Lys(Boc)-OH tetrapeptide, which was obtained from Phe-Isox-$\beta^{2,2}$-azido coupling to protected Thr and Lys, followed by Staudinger reduction of the azide ($N_3 \rightarrow NH_2$) and subsequent Fmoc protection.[32] This route needed multiple purification steps, including the separation of the resulting diastereoisomers before starting the solid-phase peptide synthesis (SPPS). Such steps could be avoided in the newly full-solid-phase procedure developed for **β-FH1** and **β-FH2**. Finally, the two diastereoisomeric peptidomimetics were then separated and purified by semipreparative HPLC. Based on **β-HM2** and its derivative, we had anticipated that the two diastereomers would adopt distinct conformations and therefore exhibit different HPLC retention times, enabling their direct separation during the final post-cleavage purification step following the solid-phase synthesis.

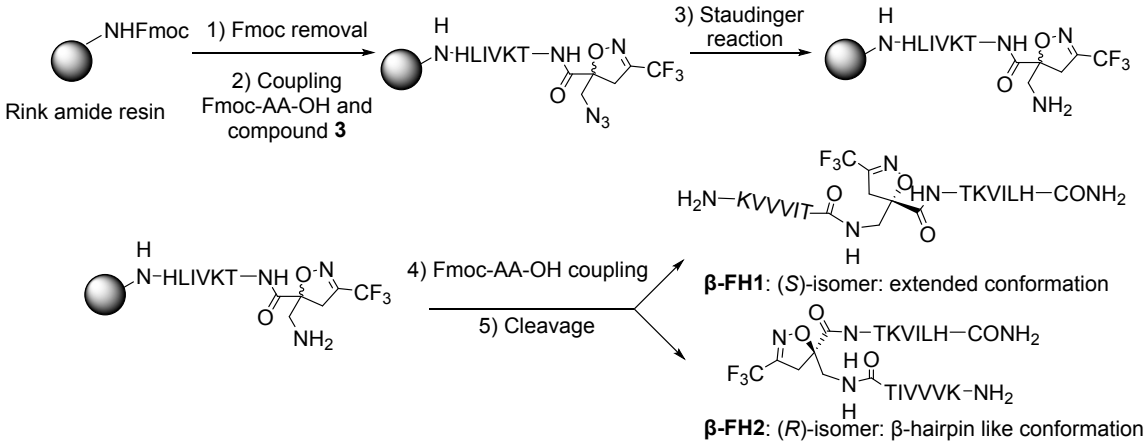

Scheme 2. Solid-phase synthesis of peptidomimetics **β-FH1** and **β-FH2. 1) Fmoc removal:** 20 % Piperidine in DMF (v/v), rt, 30 min. **2) Fmoc-AA-OH coupling**: Fmoc-AA-OH (5 eq.), HCTU (5 eq.), NMM 20 % in DMF, rt, 30 min. **Compound 3 coupling:** DIC (2 eq.) Oxyma (2 eq.), **3** (2 eq.), DMF, rt, 16 h. **3) Staudinger reaction**: $P(Me)_3$ in toluene 1 M (7 eq.) and H_2O (49 eq.) in THF or DMF, rt, 16 h. **4) Fmoc-AA-OH coupling:** Fmoc-AA-OH (5 eq.), HCTU (5 eq.), NMM 20 % in DMF, rt, 30 min. **5) Cleavage**: TFA/H_2O/TIPS/Phenol; 90/5/2.5/2.5, rt, 2h.

Conformational studies

To investigate the conformational preferences of the two peptidomimetics **β-FH1** and **β-FH2**, we employed a comprehensive suite of spectroscopic techniques, including NMR (^{1}H, ^{13}C, ^{19}F, and 2D experiments), circular dichroism (CD), and infrared (IR) spectroscopy.

Due to the low water solubility of peptidomimetic **β-FH1** and **β-FH2**, complete NMR characterization was performed in CD_3OH, including ^{1}H NMR (600 MHz), ^{13}C NMR (150 MHz), ^{19}F NMR (564 MHz) and a full set of 2D experiments (HSQC, HMBC, COSY, TOCSY, NOESY, and ROESY). Proton resonance assignments were achieved for both **β-FH1** and **β-FH2** based on 2D TOCSY and NOESY data. The chemical shift assignments are summarized in Table S3 and Table S4 (Supporting Information (SI)).

By analogy with our previous work on **β-HM2** (Isox in the *R* configuration), which showed higher HPLC retention time than its diastereomeric analogue (Isox in the *S* configuration), we hypothesized that **β-FH1** (lower HPLC retention time) corresponded to the compound featuring the *S*-Isox, whereas **β-FH2** (higher HPLC retention time) corresponded to the *R*-Isox featuring analogue.

The ^{1}H NMR spectrum of **β-FH1,** displayed quite good dispersion of the NH chemical shifts (Fig S9, SI), particularly outside the central region containing the non-natural amino acid sequence (Thr_6–$Isox_7$–Thr_8), where $^3J_{NH\text{-}H\alpha}$ values ranged from 7.2 to 6.4 Hz. At the *N*- and *C*-terminal regions, coupling constants were slightly higher (9–8 Hz and 7.8–7.4 Hz, respectively). These values align with the characteristics of extended folded structures (*J* = 8-9 Hz), although they are slightly reduced in the *C*-terminal arm. Positive deviations ($\Delta\delta$ H_α = + 0.1–0.2 ppm) from random coil chemical shifts further supported this interpretation.[59] The deviation observed for His_{13} suggests

View Article Online DOI: 10.1039/D5OB00975

increased mobility of the *C*-terminal amino acid (**Fig. 4C**). The formation of an extended conformation was further corroborated by the absence of inter-strand ROEs; only a complete set of strong CH/NH (i, i+1) ROEs was observed (**Fig. 4A** and Fig. S10 in SI). The ^{19}F NMR spectrum showed several peaks among which two main at -68.07 and -68.11 ppm in a 1:4 ratio at 278 K with much lower intensity compared to the TFA signal (Fig. S21a, SI). This can be attributed to the poor solubility of the compound and the presence of several conformers, together with an overrepresentation of residual TFA relative to the compound.

^{1}H NMR spectra of peptidomimetic of **β-FH2** were first recorded in CD_3OH at different temperatures. At 273 K, extensive overlap of NH resonances indicated two conformations in a similar ratio (Fig. S31, SI). Upon heating to 313 K, NH signal dispersion improved, although many signals remained partially overlapped; two isomers were still apparent, with one becoming predominant (~4:1 ratio, Fig. S11, SI). At 323 K, the minor conformer decreased further (Fig. S29, SI). Balancing temperature with NH resolution, **β-FH2** was characterized at 313 K, enabling assignment of each chemical shift for the main conformer (Table S4, SI). The ^{19}F NMR spectrum showed two main signals at −68.18 and −68.28 ppm in a 1:4 ratio (Fig. S34, SI). These observations are consistent with the presence of two conformers.

The extended conformation of both arms was confirmed by the positive difference observed between experimental H_α chemical shift values and "random" coil values (**Fig. 4C**). All amino acids had a positive Δδ> 0.2 for all AAs of the *N*-terminus arm) with higher values compared to those observed for **β-FH1**. In this case too, the Δδ for His_{13} is negative. The main diversity between the two peptidomimetics lay in the Δδ negative value for $Isox_7$ and Thr_8, suggesting a conformational shift with respect to **β-FH1** in this region. The turn conformation induced by the *R*-β^{2,2}-Isox moiety was supported by the presence of diastereotopic CH_2NH protons (δ 3.98, 3.76), absent on the peptidomimetic **β-FH1** (δ 3.83, brs).

The NOESY experiment revealed a complete set of strong/medium sequential CH/NH (*i*, *i+1*) NOEs for both peptide arms (**Fig. 4B** and Fig. S12-S13, SI). Notably, there is spatial proximity between NH_{Thr8} with both NH_{Lys9} (*i*,*i*+1) and NH_{Isox7} (inter-strand NOE; Fig. S15, SI). Accordingly, it can be assumed that these three NHs are oriented within the turn, as also supported by the inter-strand NOEs of $NH_{Isox7}/H_{β\text{-}Lys9}$ and $NH_{Lys9}/H_{α\text{-}Thr6}$ (tentatively assigned due to overlapped signals). A further inter-strand NOEs is that of NH_{Val3} and $H_{α\text{-}Ile11}$ (**Fig. 4B** and Fig. S13-S14, SI).

A DMSO-d_6 titration experiment was also performed to validate the formation of H-bonds (**Fig. 4D**). The combination of CD_3OD and DMSO is not ideal for titration experiments due to potential solvent interactions that may interfere with accurate measurements or disrupt hydrogen bond evaluation.[60]

In our study, significantly lower values were observed for all NHs when compared to those obtained using an aprotic solvent combined with DMSO. Given that, generally, the NHs at the *N*- and *C*-termini are not involved in hydrogen bonding, their Δδ values (ranging from 0.111 to 0.068) were used as a reference point to identify NHs not participating in a H-bond. Our hypothesis was that NHs of Thr_8 (Δδ = 0.008), Lys_9 (Δδ = 0.015) and Ala_3 (Δδ = 0.035) may form from strong to medium H-bonds. More specifically, a β-turn was formed in which $C{=}O_{Ile5}$ at position *i* forms a H-bond with NH_{Lys9} at position (*i*+3). Given the shared orientation of NHs in Lys-9 and Thr-8, we can assume that the same carbonyl also participates in a second H-bond with NH_{Thr8}. A third, weaker H-bond was formed between NH_{Ala3} with $C{=}O_{Ile11}$, consistent with the NOE observed between this NH and $H_{α\text{-}Ile11}$.

We took advantage of the presence of fluorine and its high NMR sensitivity to probe spatial proximities by ^{1}H-^{19}F measurements and thereby assess peptidomimetics conformation in CD_3OH (Fig. S35, SI). As expected, for **β-FH2**, correlations were detected between the CF_3 group and the CH_2 of the isoxazoline, as well as with the CH_3 groups of Thr_6 and Thr_8 (δ = 1.16 ppm) and other aliphatic CH_3 signals (δ ≈ 0.85 ppm, Ile or Val), confirming the β-hairpin conformation. By contrast, these correlations were not observed for the *S*-Isox analogue, **β-FH1**, consistent with a more extended conformation (Fig. S21b, SI).

Even though the *R*-Isox moiety induces the formation of a couple of conformers, we can conclude that its ability to form a β-turn supports the formation of β-hairpin populations.

Circular Dichroism (CD) experiments were first performed in phosphate buffer, the medium used to analyze the parent peptidomimetic **β-FM2,** displaying a positive maximum near 190 nm and a minimum around 220 nm, indicative of a stronger β-sheet/β-hairpin propensity.[32]

Nevertheless, due to the aggregation tendency of both **β-FH1 and β-FH2** in phosphate buffer, we moved to water. **β-FH1** was analyzed at a concentration of 125 µM, operating at 25 °C but the voltage of the light ray for **β-FH1** was excessively high, indicating that the sample was not completely dissolved, even though the solution appeared transparent. Consequently, the sample was diluted to 62.5 µM.

Under these conditions, **β-FH1** displayed a dominant negative absorption signal around 200 nm, consistent with a predominantly random-coil ensemble. In contrast, **β-FH2** showed an overall weaker CD response, along with a slight minimum at 220 nm. Based on these findings, we hypothesize that the random coil structure characterized both samples. However, the minimum at 220 nm, indicative of a β-sheet structure, is more pronounced for **β-FH2** (**Fig. 5**), as evidenced by the ellipticity ratio of the two minima in the two samples.

Because **β-FH2** had to be measured in water, a direct quantitative comparison with **β-HM2** is not fully reliable, but some conclusions can be taken. Nevertheless, the CD data suggest that **β-FH2** is less strongly β-structured than **β-HM2** in aqueous solution, while still showing a slightly higher β-sheet propensity than **β-FH1**.

ATR-FTIR spectra (amide I region) were next used to further probe the secondary-structure preferences of the peptidomimetics in the solid state, and comparison with the parent **β-HM2** were reported. Deconvolution indicated that both **β-FH1** and **β-FH2** predominantly populate β-type

View Article Online
DOI: 10.1039/D6OB00187D

conformations, in line with the β-rich profile previously reported for **β-HM2**.

For **β-HM2**, amide-I fitting indicates a conformational distribution dominated by β-sheet (47%) and β-turn (30%), with minor contributions from random structures (15%) and β-aggregated strands (8%).[32]

Similarly, **β-FH1** displayed a strong β contribution, with bands at 1630 cm^{-1} (33%, β-sheet) and 1700 cm^{-1} (13%, antiparallel β-sheet), together with 1687 cm^{-1} (26%, β-turn) and a substantial 1664 cm^{-1} component (28%, assigned to a 3_{10}-helix) (**Fig. 6A**). Notably, the band at 1700 cm^{-1}, commonly associated with antiparallel β-sheet, is consistent with the extended conformation inferred from NMR in solution and with the aggregation propensity observed by CD and ThT assays (**Fig. 7a**, **Fig. 7b**).

In contrast, **β-FH2** exhibited an even stronger β-sheet signature, with a dominant component at 1631-1632 cm^{-1} (55%, β-sheet), accompanied by 1672 cm^{-1} (26%, β-turn) and a pronounced low-frequency contribution at 1600 cm^{-1} (19%) attributed to aggregated strands (**Fig. 6B**). Compared with **β-HM2**, **β-FH2** therefore shows both a higher β-sheet content and a markedly enhanced aggregation component, in line with its limited solubility.

Taken together, these data indicate that the **β-FH** series retains the β-rich character of **β-HM2**, while shifting the balance toward either mixed conformations (**β-FH1**, including a 3_{10} component) or enhanced β-sheet/aggregation features (**β-FH2**).

View Article Online
DOI: 10.1039/D6OB00187D

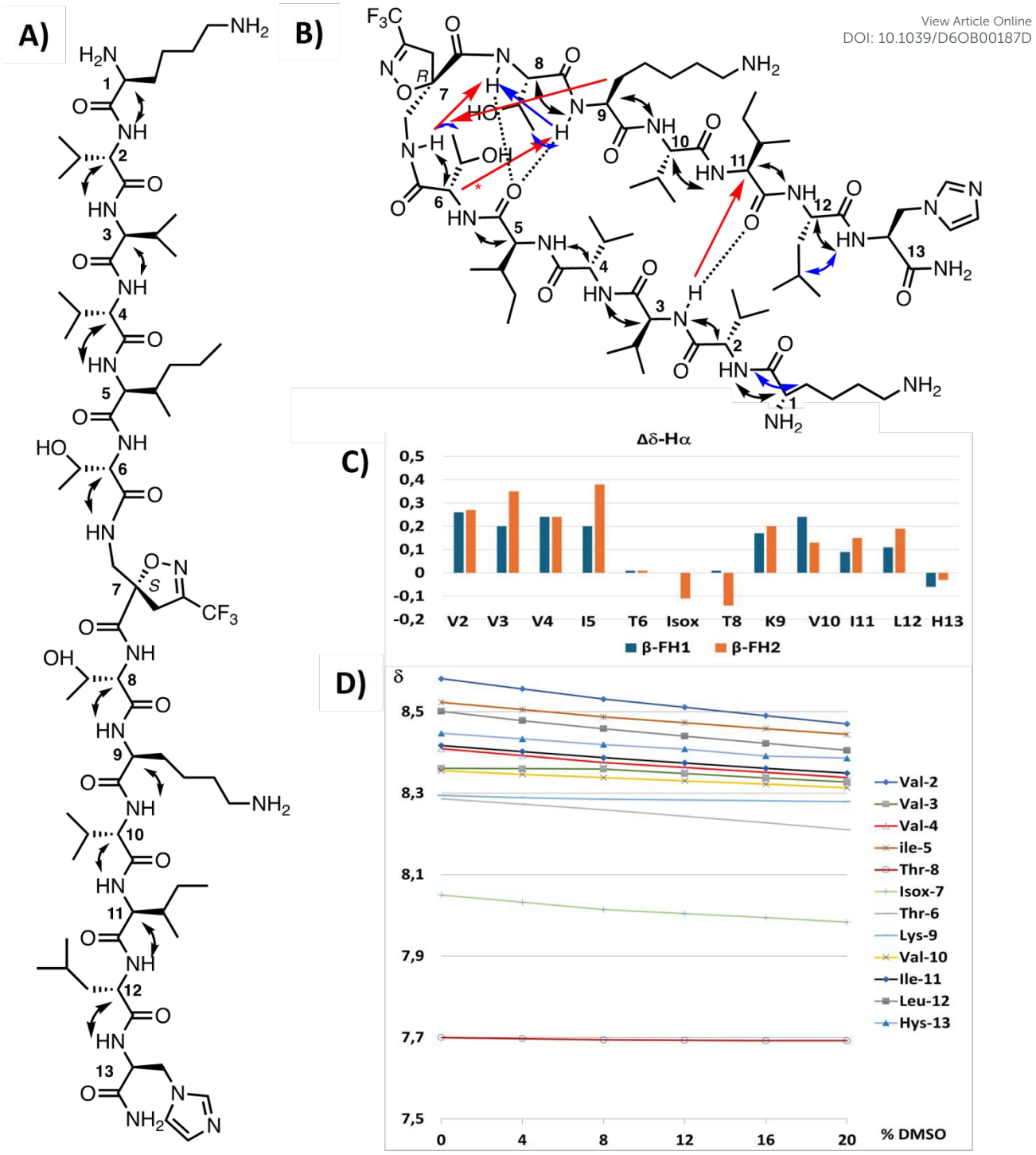

Fig. 4. ROEs (CD_3OH, 4.0 mg in 750 µL, T = 298K) and NOEs (CD_3OH, 4.1 mg in 750 µL, T = 313K) for **A) β-FH1** and **B) β-FH2**, respectively (Black: CH_α/NH (*i*, *i+1*) NOEs; Blue: NH/NH or $CH_{\beta/\gamma}$/NH (*i*, *i+1*) NOEs; Red: intra-strand NOEs); *Tentatively assigned. **C)** Δδ of H_α relative to random coil of peptidomimetics **β-FH1** and **β-FH2** (the Δδ value for Isox in peptidomimetic **β-FH2** is referred to the same proton in **β-FH1**).[61] **D)** Plots of the chemical shifts of NH groups in the ^1H NMR spectra of **β-FH2** dissolved in CD_3OH (3.61 mg in 660 µL, T = 313 K) with the addition of increasing DMSO amounts (0, 4, 8, 12, 16, 20 %).

View Article Online
DOI: 10.1039/D6OB00187D

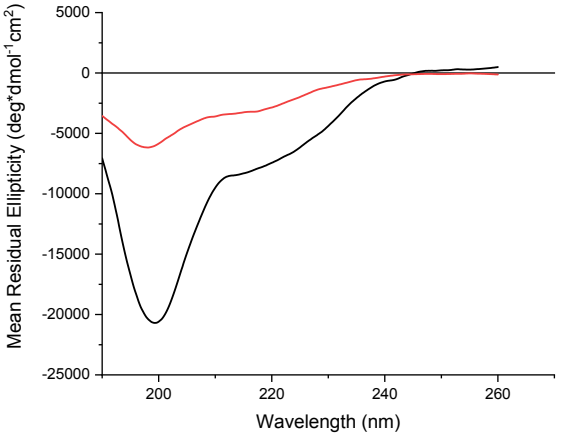

Fig. 5. Far UV CD spectra at room temperature in H_2O of peptidomimetics **β-FH1** (62.5 µM; black line) and **β-FH2** (125 µM; red line) at 25°C.

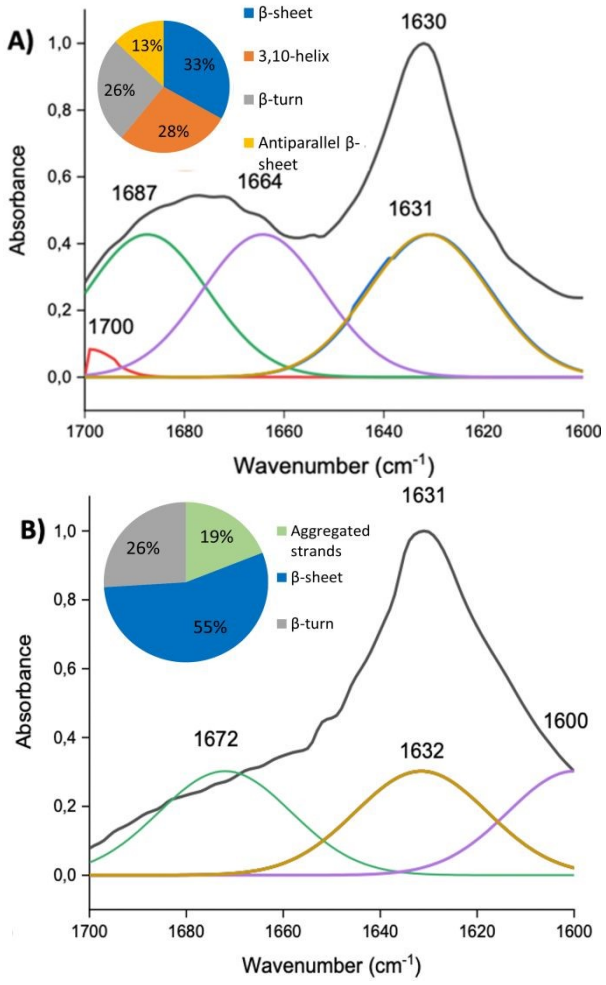

Fig. 6. Deconvoluted FT-IR spectra in the solid state of **A) β-FH1** and **B) β-FH2** (62.5 µM in H_2O). The grey-line indicates the original FT-IR spectra and the colored lines represent the deconvoluted curves with a Gaussian function (Data processing was performed using solver in excel software (Microsoft).

Effect of β-FH1 and β-FH2 on Tau aggregation

β-FH1 and **β-FH2** were assessed for their ability to modulate fibrillization of full-length Wt-Tau441 and the pro-aggregative Tau-ΔK280 variant using ThT fluorescence spectroscopy and TEM (**Fig. 7**). Methylene blue (**MB**), a well-characterized Tau aggregation inhibitor that has advanced to phase II clinical trials for Alzheimer's disease, served as a reference control to benchmark inhibitory activity. Its well-documented efficacy against Tau fibrillization made MB a robust positive control in both ThT and TEM assays, enabling direct comparison and validation of the anti-aggregation properties of our peptidomimetics (**Fig. 7** and Fig. S6).[62–65]

In ThT assays, anionic cofactors were required to initiate the aggregation. Under our conditions (5 µM protein in 25 mM NaPi, 25 mM NaCl, 2.5 mM EDTA, pH 6.8), the minimal heparin concentration yielding robust and highly reproducible aggregation for our Wt-Tau441 batch was 0.5 µM (Tau/heparin = 10/1; Fig. S5).[66–68] Because fibrillization proceeded rapidly after cofactor addition, protein and compounds were pre-incubated for 1 h prior to heparin addition.

ThT kinetics indicated that **β-FH1** displayed an erratic behavior and a strong self-aggregation upon heparin addition that impaired fluorescence readouts (light blue and orange curves for 25 µM, 10 µM, respectively, **Fig. 7a,** left). Indeed, in the presence of **β-FH1** and Wt-Tau441, the ThT fluorescence (F) remained very high at an inhibitor/Tau ratio of 5/1 and 2/1 (dark blue and green curves, **Fig. 7a**), suggesting pronounced self-aggregation. This aggregation interferes with ThT-based measurements and thus prevents reliable evaluation of the inhibitory effects of **β-FH1** on Wt-Tau441 and Tau-ΔK280 fibrillization (**Fig. 7a** and **b**, left). This behavior is likely related to the extended conformation adopted by **β-FH1**, which may promote intermolecular interactions.

By contrast, **β-FH2** showed no evidence of the heparin-induced self-aggregation and exhibited a strong suppression of ThT fluorescence signal. **β-FH2** totally inhibited Wt-Tau441 fibrillization at 5/1 ratio and significantly decreased the signal at 2/1 ratio (ΔF = 44.4±8.0% relative to Tau control; **Fig. 7a**, right, Table S1, SI). Similar results were observed with Tau-ΔK280 mutant, showing complete inhibition of the ThT fluorescence signal at an inhibitor/Tau ratio of 5/1 and a reduction by 86.2±6.6% at a 2/1 ratio (**Fig. 7b**, right, Table S2, SI).

As expected, **MB** inhibited Wt-Tau441 fibrillization in a concentration-dependent manner. The residual ThT signal decreased to 6.0±0.6%, 21.3±2.1% and 32.2±2.6% at **MB**/Tau ratios of 5/1, 2/1, and 1/1, respectively (Fig. S6, Table S1, SI), displaying a greater activity than **β-FH2** but remaining in the same range. Similar inhibition trends were obtained with Tau-ΔK280 at ratios 5/1 and 2/1 (Fig. S7, Table S2, SI).

To complement the ThT kinetics and resolve the apparent heparin-triggered self-aggregation of **β-FH1**, we performed TEM to directly visualize Tau aggregate morphology. Accordingly, TEM micrographs of Wt-Tau441 and Tau-ΔK280

View Article Online
DOI: 10.1039/D6OB00187D

were acquired after heparin-induced aggregation in the absence or presence of **β-FH1**, **β-FH2**, or **MB** at a 5/1 ratio, the concentration used in the fluorescence assay displaying the greater effects.

As expected, in the presence of heparin, Wt-Tau441 produced long and homogenously distributed fibrils (length ~6 µm, width ~16 nm, **Fig. 7c**, image 1). Addition of **β-FH1** to Wt-Tau441 produced shorter, markedly denser fibrils, consistent with a pro-aggregative effect under these conditions (length ~ 300-500 nm, width ~ 17 µm, **Fig. 7c**, image 2). This effect may be explained by the extended conformation adopted by the compound, which could facilitate nucleation and promote denser fibril formation. However, no fibrils or aggregates of **β-FH1** alone were detected in the presence of heparin, potentially reflecting the formation of sub-resolvable fibrillar species, which are nevertheless able to interact with ThT (Fig. S8, a) and c), SI).

TEM micrographs of Tau in the presence of **β-FH2** revealed a drastically different morphology of the fibers network, composed of significantly shorter and abundant, fibrillar fragments than for Tau control, with assemblies that were predominantly truncated and clustered, consistent with altered aggregation pathway (**Fig. 7c**, image 3).

By contrast, **MB** (ratio 5/1) mainly altered Wt-Tau441 fibers length. While a few long fibrils persisted, the dominant population comprised markedly shorter fibrils (~100 nm) with comparable widths (~18-20 nm) (**Fig. 7c**, image 4, **MB**) to Wt-Tau441 control, consistent with a potent inhibition of fibril elongation or enhanced fragmentation at this ratio.

For Tau-ΔK280, the control images exhibited short fibrillar assemblies rather than long, dispersed filaments (**Fig. 7d**, image 1) as observed for the Wt-Tau441 control. In the presence of **β-FH1** or **β-FH2**, fibrils are less dispersed and markedly enriched in focal clusters, consistent with locally catalyzed aggregation and in line with the morphology observed for Wt-Tau441 (**Fig. 7d,** images 2 and 3); the network being denser for **β-FH1** than for **β-FH2**.

β-HM2, the parent scaffold from which **β-FH1** and **β-FH2** are derived, was previously reported to fully inhibit Wt-Tau/heparin aggregation at an inhibitor/Tau ratio of 5/1 (and also at 1/1), as shown by ThT-fluorescence and TEM. At a sub-stoichiometric ratio (0.1/1), **β-HM2** no longer inhibited aggregation and yielded ThT kinetics comparable to the Tau/heparin control. Notably, TEM nevertheless revealed a pronounced shift toward short, straight fibrillar species, a morphology qualitatively reminiscent of that observed for **β-FH1** and **β-FH2** at substantially higher inhibitor ratio (5/1).

β-HM1, which features the same key Hsp90-derived sequences, primarily stabilized non-fibrillar, rod-like nanostructures that were not detected in the ThT assay. By TEM, these assemblies appeared as short rods with nm-scale widths (~16–19 nm) and, in some cases, partially open morphologies suggestive of intermediate-like architectures. Together, these TEM data suggest that **β-HM1** acts by stabilizing intermediate assemblies,[32] whereas **β-FH1** and **β-FH2** remodel fibrillar assembly toward shorter and more clustered fibrillar species rather than preventing fibril formation.

However, comparisons of the effects of these compounds **β-HM1/2** *vs* **β-FH1/2** on Tau aggregation must be made with caution, as the experimental conditions are not identical. Indeed, the ratio of Tau/heparin used varies greatly (10/1 in this study *vs* 160/1 and 4/1 for ref. 31 and 100/1 for ref. 32), as do the concentrations (5 *vs* 10 µM) and batches of Tau used.

View Article Online
DOI: 10.1039/D6OB00187D

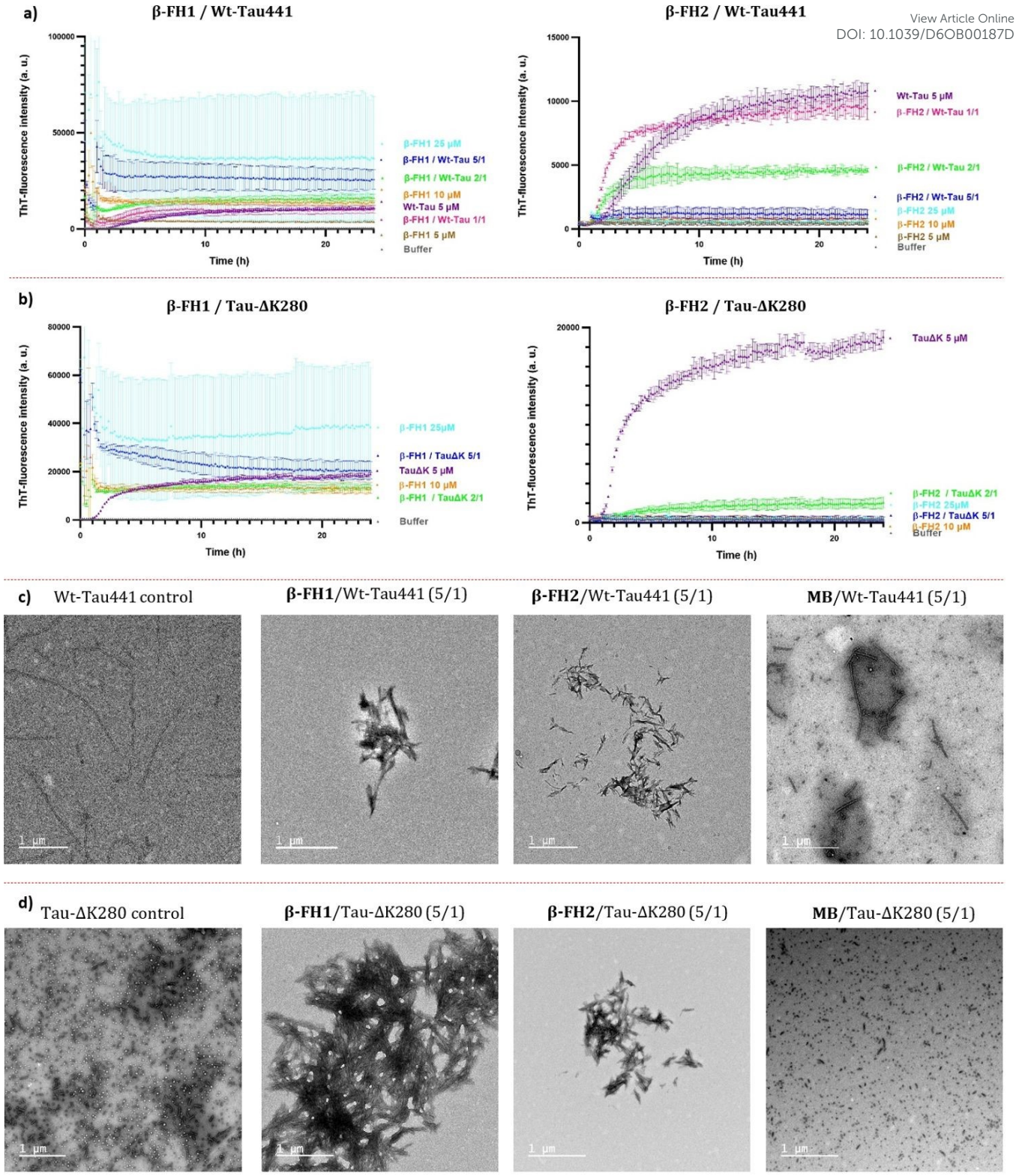

Fig. 7. Curves of ThT fluorescence assays over time in the absence (purple curve) and in the presence of **β-FH1** or **β-FH2** at compound/Tau ratios of 5/1 (dark blue curves), 2/1 (green curves), and 1/1 (pink curves) for **a)** Wt-Tau441 and **b)** Tau-ΔK280 (only ratios 5/1 and 2/1) fibrillization (5 µM for both) represented as a mean (triplicate±SD) and expressed as arbitrary units (a.u). The control curves of the compounds are represented in light blue (25 µM), orange (10 µM) and brown (5 µM) and the buffer in grey. **c, d)** Transmission electron micrographs, Wt-Tau441 and Tau-ΔK280 alone (control) and in the presence of **β-FH1**, **β-FH2** and positive control **MB** (5/1 ratios). Samples were negatively stained with 2% (w/v) phosphotungstic acid (PTA), pH ~7.0, and imaged using a transmission electron microscope at 120 kV. Scale bars = [1 µm].

DOI: 10.1039/D6OB00185D

Tau–Microtubule dynamics in the FDAP cell-based assay in the presence of β-FH1 and β-FH2

Because the fibrils formed in the presence of our compounds displayed markedly altered morphologies, we next asked whether they might also reduce Tau aggregation and potentially restore Tau-microtubule (Tau-Mt) engagement in cells. To address this, we performed quantitative live-cell FDAP (fluorescence decay after photoactivation) assays in model neurons. A defined subpopulation of PAGFP (photoactivatable GFP)-tagged aggregation-prone Tau-ΔK280 was photoactivated in axon-like processes of neuronally differentiated PC-12 cells, and the ensuing fluorescence decay was analyzed to quantify Tau–microtubule interaction kinetics (**Fig. 8**).[69–74]

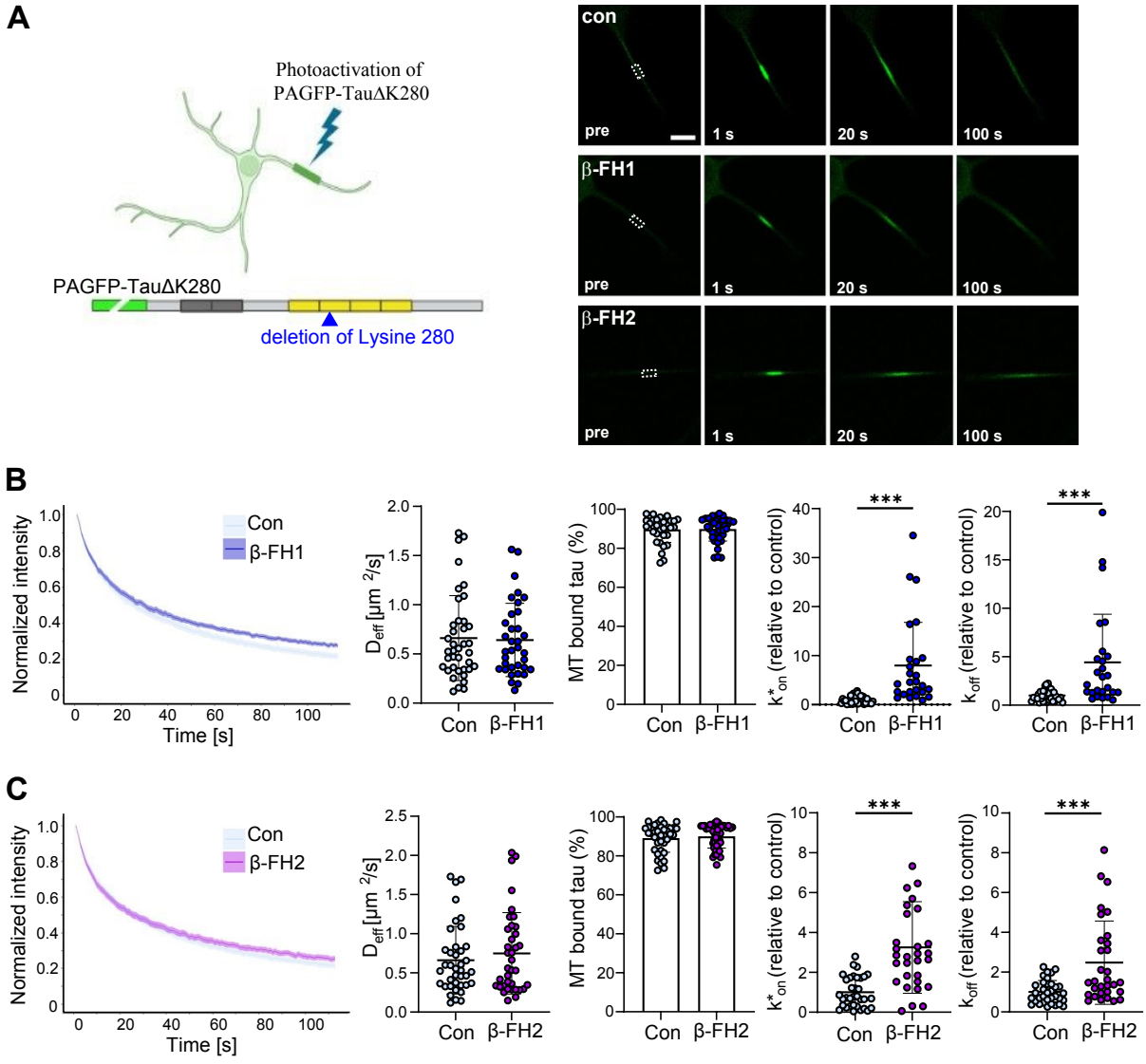

Fig. 8. Fluorescence decay after photoactivation (FDAP) analysis of the interaction of Tau with microtubules in axon-like processes of model neurons. **A)** Schematic representation of the experimental approach. Aggregation-prone Tau (Tau-ΔK280), aminoterminally tagged with photoactivatable GFP (PAGFP), is expressed in neuronally differentiated PC12 cells. Photoactivation is performed in the middle of the process, and the fluorescence decrease is recorded as an indicator of microtubule interaction. Representative time-lapse micrographs of a FDAP experiment are shown on the right. Scale bar: 10 µm. The activation and recording region are indicated in the pre-activation image (6 µm length). **B-C)** FDAP plots of PAGFP-tagged Tau-ΔK280 and scatter plots of the effective diffusion constants (Deff), the amount of tau bound to microtubules, and the association (k*on) and dissociation rate constants (koff) in the presence of **β-FH1** (B) and **β-FH2** (C) compared to untreated control. Mean±SEM of 39 (control), 35 (25µM β-FH1), and 37 cells (25 µM β-FH2) are shown. Statistically significant differences between samples, determined by unpaired two-tailed Student's tests, are indicated. ***p<0.001. Incubation with the substance lasted 20 hours in all experiments.

View Article Online
DOI: 10.1039/D6OB00187D

Neither **β-FH1** nor **β-FH2** affected the mobility of the aggregation-prone Tau protein (Tau-ΔK280), as shown by the unchanged effective diffusion constant (Deff) in axon-like processes (**Fig. 8**). Accordingly, the proportion of Tau protein bound to microtubules remained unchanged, suggesting that the two compounds did not reduce Tau aggregation, which would have led to increased Tau binding to microtubules. However, application of a refined reaction–diffusion model of the Tau–microtubule interaction[71] revealed significant increases in the apparent association and dissociation rate constants of Tau binding (k*on and koff). The results suggest that **β-FH1** and **β-FH2** penetrate the cells and influence the Tau–microtubule interaction, but do not reduce the formation of Tau aggregates.

The toxicity of compounds **β-FH1** and **β-FH2** alone was evaluated using an MTT cell viability assay across a range of concentrations up to 100 µM. The compounds do not impair PC-12 cell viability, even at the highest concentration tested (Figure S37, SI). This concentration is four times higher than the concentration at which the FDAP analysis was performed.

Proteolytic stability assays

Finally, the resistance of the compounds to proteolytic degradation was assessed in a Pronase E challenge assay. Each compound was solubilized at 200 µM and incubated with Pronase E (2.5 µg/mL). Proteolysis was followed over 2 h by RP-HPLC-MS, which also allowed the main cleavage events to be mapped. Both compounds exhibited excellent stability in this broad-spectrum enzymatic medium, with 98% of **β-FH1** and 95% of **β-FH2** remaining intact after 2 h, indicating a very strong resistance to proteolysis. The primary cleavage sites are shown in Fig. S2 and Fig. S4.

Conclusions

The replacement of the phenyl group in **β-HM2** with a **trifluoromethyl** substituent in Isox-$\beta^{2,2}$-AA based peptidomimetics had a major impact on both the conformation and the activity of small synthetic chaperones designed to mimic the physiological Hsp90. The fluorinated **β-FH1** (*S*-Isox) preferentially adopts an extended conformation, whereas **β-FH2** (*R*-Isox) favors a β-hairpin-like conformation. However, this β-hairpin is less stable than those observed for **β-HM1** and **β-HM2** as demonstrated by NMR and CD analyses.

Furthermore, **β-FH1** and **β-FH2** showed an increased tendency to self-associate, as reflected by their poor solubility in polar solvents (in contrast to **β-HM1** and **β-HM2**, which could be analyzed in phosphate buffer) and by ATR-FTIR, which indicates that **β-FH2** adopts a denser, more tightly packed β-structured/aggregated organization in the solid state than **β-HM2**. Consistent with these physicochemical and conformational changes, **β-FH2** displayed a loss of activity toward Tau aggregation relative to **β-HM1** and **β-HM2**, as evidenced by TEM and FDAP-based cellular assays.

Replacing phenyl with CF_3 primarily alters the electron field and the local geometry: CF_3 exerts a strong inductive (–I) effect and introduces a large local dipole while being compact. Phenyl, in contrast, is bulkier and anisotropic, providing mainly a steric hindrance and dispersion contacts. In **β-FH2**, the CF_3 field modifies the local electronic and steric environment, which may perturb the β-hairpin hydrogen-bonding network. These changes are consistent with a less constrained hairpin conformation and potentially increased conformational dynamics. This conformational plasticity may be associated with the dense fibrillar clustering, as observed by TEM. In this context, **β-FH2** still shows partial activity against Tau in ThT assays, but this readout may be influenced by the presence of self-associated **β-FH2** species which could contribute to the observed aggregation behavior. These assemblies could divert Tau into an aggregation pathway distinct from Tau alone, yielding more clustered and fragmented morphologies (TEM). Importantly, this remodeled aggregation state appears incompatible with restoring Tau-microtubule binding in cells, in contrast to **β-HM1** and **β-HM2**, whose more constrained β-hairpin presentation supports more effective functional recovery.

Overall, this study provides additional information on the mechanism by which small-molecule Hsp90 mimics may influence Tau aggregation, suggesting the requirement for a β-hairpin conformation to properly display the key S4 and S7 sequences of Hsp90 and thereby interfere with Tau misfolding and the intra- and intermolecular interactions that drive maturation into fibrils. We can also hypothesize that the lack of activity stems from the absence of an aromatic moiety required to perturb Tau aggregation, as previously observed for Aβ with the piperidine–pyrrolidine scaffold, where the tosyl group proved critical: removing it or replacing it with a Boc group led to a dramatic loss of inhibitory efficiency.[75]

Nevertheless, because this new scaffold can promote either an extended conformation (*S*-Isox) or a folded hairpin-like conformation (*R*-Isox), and as its introduction in peptide containing 13 residues dramatically protects this peptidomimetic from the proteolysis, this scaffold may warrant further exploration in other areas of medicinal chemistry. The trifluoromethyl group could also be used as a probe to investigate biological processes and the interaction of peptides including this fluorinated Isox-$\beta^{2,2}$-AA with various biological targets by ^{19}F-NMR spectroscopy.

Author contributions

T.M., M.-L.G., and S. O. designed the compounds and experiments. M.S. and C.V. performed the synthesis under the supervision of T.M. and S.O.. M.-L.G and K.P. performed the conformational analysis by NMR, IR, and CD. A. W. and L.S., performed the MTT assays and quantitative live-cell imaging under the supervision of R. B.. M. S. and J. K. performed the ThT fluorescence and TEM assays. V.C. and B.G. performed the production of Tau protein. F.G. performed the ^{19}F-NMR analysis. All authors participated to the writing of the manuscript. All authors have given approval to the final version of the manuscript.

Conflicts of interest

There are no conflicts to declare.

Data availability

The data supporting this article have been included as part of the supplementary information (SI). Supplementary information is available.

Acknowledgements

This work is funded by the ANR FluFOLD N° ANR-22-CE44-0020-01 (PhD funding of MS and experimental costs). This study was supported by funds from University of Milan - Piano di sostegno alla Ricerca 2025 - LINEA 2

The present work has benefited from Imagerie-Gif core facility supported by l'Agence Nationale de la Recherche (FBI ANR-24-INBS-0005 (BIOGEN); SPS ANR-17-EUR-0007, EUR SPS-GSR.

The authors warmly thank Lydia Hassissene (I2BC) for her assistance and expertise with TEM experiments and Karine Leblanc (BioCIS) for the technical support and help with peptide purification and mass spectrometry analysis.

The authors gratefully acknowledge Central Glass Co. for the gift of trifluoroacetaldehyde hydrate.

Notes and references

1 A. Nandi, N. Counts, J. Bröker, S. Malik, S. Chen, R. Han, J. Klusty, B. Seligman, D. Tortorice, D. Vigo and D. E. Bloom, *npj Aging*, 2024, **10**, 1–8.
2 S. Dhillon, *Drugs*, 2021, **81**, 1437–1443.
3 C. H. Van Dyck, C. J. Swanson, P. Aisen, R. J. Bateman, C. Chen, M. Gee, M. Kanekiyo, D. Li, L. Reyderman, S. Cohen, L. Froelich, S. Katayama, M. Sabbagh, B. Vellas, D. Watson, S. Dhadda, M. Irizarry, L. D. Kramer and T. Iwatsubo, *N. Engl. J. Med.*, 2023, **388**, 9–21.
4 M. H. Ebell, H. C. Barry, K. Baduni and G. Grasso, *Ann. Fam. Med.*, 2024, **22**, 50–62.
5 A. Mullard, *Nature Reviews Drug Discovery*, 2023, **22**, 89–89.
6 European Medicines Agency (EMA), Leqembi recommended for treatment of early Alzheimer's disease, 2024, https://www.ema.europa.eu/en/news/leqembi-recommended-treatment-early-alzheimers-disease.
7 J. R. Sims, J. A. Zimmer, C. D. Evans, M. Lu, P. Ardayfio, J. Sparks, A. M. Wessels, S. Shcherbinin, H. Wang, E. S. M. Nery, E. C. Collins, P. Solomon, S. Salloway, L. G. Apostolova, O. Hansson, C. Ritchie, D. A. Brooks, M. Mintun, D. M. Skovronsky, *JAMA*, 2023, **330**, 512–527.
8 S. Reardon, *Nature*, 2024, https://doi.org/10.1038/d41586-024-01726-w
9 U.S. Food and Drug Administration, FDA approves treatment for adults with Alzheimer's disease, 2024, https://www.fda.gov/drugs/news-events-human-drugs/fda-approves-treatment-adults-alzheimers-disease.
10 P. Barbier, O. Zejneli, M. Martinho, A. Lasorsa, V. Belle, C. Smet-Nocca, P. O. Tsvetkov, F. Devred and I. Landrieu, *Front. Aging Neurosci.*, 2019, **11**, 204.
11 Y. Zhang, K.-M. Wu, L. Yang, Q. Dong and J.-T. Yu, *Mol. Neurodegeneration*, 2022, **17**, 28.
12 J. Zhang, Y. Zhang, J. Wang, Y. Xia, J. Zhang and L. Chen, *Sig. Transduct. Target. Ther.*, 2024, **9**, 1–35.
13 M. V. Alstyne, J. Pratt and R. Parker, *Genes Dev.*, 2025, **39**, 555–581.
14 S. Altinok, R. Sanchez-Hodge, M. Stewart, K. Smith and J. C. Schisler, *Cells*, 2021, **10**, 3121.
15 A. Wentink, C. Nussbaum-Krammer and B. Bukau, *Cold Spring Harb. Perspect. Biol.*, 2019, **11**, a033969.
16 J. Tittelmeier, E. Nachman and C. Nussbaum-Krammer, *Front. Aging Neurosci.*, 2020, **12**, 581374.
17 C. L. Klaips, G. G. Jayaraj and F. U. Hartl, *J. Cell Biol.*, 2017, **217**, 51–63.
18 M. S. Hipp, P. Kasturi and F. U. Hartl, *Nat. Rev. Mol. Cell. Biol.*, 2019, **20**, 421–435.
19 B. S. Rutledge, W.-Y. Choy and M. L. Duennwald, *J. Biol. Chem.*, 2022, **298**,101905.
20 V. N. Uversky, *Front. Aging Neurosci.* 2015, **7**, 18.
21 A. M. de Graff, D. E. Mosedale, T. Sharp, K. A. Dill and D. J. Grainger, *PLOS Comput. Biol.*, 2020, **16**, e1008460.
22 R. E. Lackie, A. Maciejewski, V. G. Ostapchenko, J. Marques-Lopes, W.-Y. Choy, M. L. Duennwald, V. F. Prado and M. A. M. Prado, *Front. Neurosci.*, 2017, **11**, 254.
23 A. Gupta, A. Bansal and K. Hashimoto-Torii, *Neurosc. Lett.*, 2020, **716**, 134678.
24 C. A. Dickey, A. Kamal, K. Lundgren, N. Klosak, R. M. Bailey, J. Dunmore, P. Ash, S. Shoraka, J. Zlatkovic, C. B. Eckman, C. Patterson, D. W. Dickson, N. S. Nahman, M. Hutton, F. Burrows and L. Petrucelli, *J. Clin. Invest.*, 2007, **117**, 648–658.
25 Z. T. Young, S. A. Mok and J. E. Gestwicki, *Cold Spring Harb. Perspect. Med.*, 2018, **8**, a024612.
26 F. H. Schopf, M. M. Biebl and J. Buchner, *Nat. Rev. Mol. Cell. Biol.*, 2017, **18**, 345–360.
27 S. Weickert, M. Wawrzyniuk, L. H. John, S. G. D. Rüdiger and M. Drescher, *Science Advances*, 2020, **6**, eaax6999.
28 L. Ferrari, R. Stucchi, K. Konstantoulea, G. van de Kamp, R. Kos, W. J. C. Geerts, L. S. van Bezouwen, F. G. Förster, M. Altelaar, C. C. Hoogenraad and S. G. D. Rüdiger, *Nat. Commun.*, 2020, **11**, 571.
29 J. Oroz, B. J. Chang, P. Wysoczanski, C.-T. Lee, Á. Pérez-Lara, P. Chakraborty, R. V. Hofele, J. D. Baker, L. J. Blair, J. Biernat, H. Urlaub, E. Mandelkow, C. A. Dickey and M. Zweckstetter, *Nat. Commun.*, 2018, **9**, 4532.
30 A. Moll, L. M. Ramirez, M. Ninov, J. Schwarz, H. Urlaub and M. Zweckstetter, *Nat. Commun.*, 2022, **13**, 3668.
31 D. Di Lorenzo, N. Bisi, J. Kaffy, L. M. Ramirez, M. Zweckstetter, O. Lequin, I. Garfagnini, J. Luo, Y. Hannappel, I. Ennen, V. Dodero, N. Sewald, M. L. Gelmi, N. Tonali, R. Brandt and S. Ongeri, *Nat. Commun.*, 2025, **16**, 8756.
32 D. Di Lorenzo, N. Bisi, R. Bucci, I. Ennen, L. Lo Presti, V. Dodero, R. Brandt, S. Ongeri, M.-L. Gelmi and N. Tonali, *iScience*, 2025, **28**, 112272.
33 X. Ran and J. E. Gestwicki, *Curr. Opin. Chem. Biol.*, 2018, **44**, 75–86.
34 E. Martino, S. Chiarugi, F. Margheriti and G. Garau, *Front. Chem.*, 2021, **9**, 718405.
35 H. Bruzzoni-Giovanelli, V. Alezra, N. Wolff, C.-Z. Dong, P. Tuffery and A. Rebollo, *Drug Discov. Today*, 2018, **23**, 272–285.
36 H. Lu, Q. Zhou, J. He, Z. Jiang, C. Peng, R. Tong and J. Shi, *Sig. Transduct. Target Ther.*, 2020, **5**, 1–23.
37 M. Pelay-Gimeno, A. Glas, O. Koch and T. N. Grossmann, *Angew. Chem. Int. Ed.*, 2015, **54**, 8896–8927.
38 J. Laxio Arenas, J. Kaffy and S. Ongeri, *Curr. Opin. Chem. Biol.*, 2019, **52**, 157–167.
39 G. E. Karagöz, A. M. S. Duarte, E. Akoury, H. Ippel, J. Biernat, T. Morán Luengo, M. Radli, T. Didenko, B. A. Nordhues, D.

B. Veprintsev, C. A. Dickey, E. Mandelkow, M. Zweckstetter, R. Boelens, T. Madl and S. G. D. Rüdiger, *Cell*, 2014, **156**, 963–974.
40 T. J. Yun, E. K. Harning, K. Giza, D. Rabah, P. Li, J. W. Arndt, D. Luchetti, M. A. Biamonte, J. Shi, K. Lundgren, A. Manning and M. R. Kehry, *J. Immunol.*, 2011, **186**, 563–575.
41 W. K. Hagmann, *J. Med. Chem.*, 2008, **51**, 4359–4369.
42 E. P. Gillis, K. J. Eastman, M. D. Hill, D. J. Donnelly and N. A. Meanwell, *J. Med. Chem.*, 2015, **58**, 8315–8359.
43 M. Inoue, Y. Sumii and N. Shibata, *ACS Omega*, 2020, **5**, 10633–10640.
44 Y. Yu, A. Liu, G. Dhawan, H. Mei, W. Zhang, K. Izawa, V. A. Soloshonok and J. Han, *Chin. Chem. Lett.*, 2021, **32**, 3342–3354.
45 C. Jäckel and B. Koksch, *Eur. J. Org. Chem.*, 2005, **2005**, 4483–4503.
46 B. C. Buer and E. N. G. Marsh, *Prot. Science*, 2012, **21**, 453–462.
47 E. N. G. Marsh, *Acc. Chem. Res.*, 2014, **47**, 2878–2886.
48 M. Salwiczek, E. K. Nyakatura, U. I. M. Gerling, S. Ye and B. Koksch, *Chem. Soc. Rev.*, 2012, **41**, 2135–2171.
49 N. C. Yoder and K. Kumar, *Chem. Soc. Rev.*, 2002, **31**, 335–341.
50 U. I. M. Gerling, M. Salwiczek, C. D. Cadicamo, H. Erdbrink, C. Czekelius, S. L. Grage, P. Wadhwani, A. S. Ulrich, M. Behrends, G. Haufe and B. Koksch, *Chem. Sci.*, 2013, **5**, 819–830.
51 E. N. G. Marsh, B. C. Buer and A. Ramamoorthy, *Mol. BioSyst.*, 2009, **5**, 1143–1147.
52 C. Dalvit and A. Vulpetti, *J. Med. Chem.*, 2019, **62**, 2218–2244.
53 C. Dalvit, A. D. Gossert, J. Coutant and M. Piotto, *Magn. Reson. Chem.*, 2011, **49**, 199–202.
54 C. Dalvit, *Prog. Nucl. Magn. Reson. Spectrosc.*, 2007, **51**, 243–271.
55 C. Dalvit and A. Vulpetti, *ChemMedChem*, 2011, **6**, 104–114.
56 Z. Chai and C. Li, *Chem. Eur. J.*, 2024, **30**, e202303988.
57 R. Bucci, F. Vaghi, D. Di Lorenzo, F. Anastasi, G. Broggini, L. Lo Presti, A. Contini and M. L. Gelmi, *Eur. J. Org. Chem.*, 2022, **2022**, e202200601.
58 R. S. B. Gonçalves, M. D. Santos, G. Bernadat, D. Bonnet-Delpon and B. Crousse, *Beilstein J. Org. Chem.*, 2013, **9**, 2387–2394.
59 D. S. Wishart, B. D. Sykes and F. M. Richards, *Biochemistry*, 1992, **31**, 1647–1651.
60 J. Kiefer, K. Noack and B. Kirchner, *Curr. Phys. Chem.*, 2011, **1**, 340–351.
61 D. S. Wishart, C. G. Bigam, A. Holm, R. S. Hodges and B. D. Sykes, *J. Biomol. NMR*, 1995, **5**, 67–81.
62 C. M. Wischik, R. T. Staff, D. J. Wischik, P. Bentham, A. D. Murray, J. M. D. Storey, K. A. Kook and C. R. Harrington, *J. Alzheimers Dis.*, 2015, **44**, 705–720.
63 S. Gauthier, H. H. Feldman, L. S. Schneider, G. K. Wilcock, G. B. Frisoni, J. H. Hardlund, H. J. Moebius, P. Bentham, K. A. Kook, D. J. Wischik, B. O. Schelter, C. S. Davis, R. T. Staff, L. Bracoud, K. Shamsi, J. M. D. Storey, C. R. Harrington and C. M. Wischik, *The Lancet*, 2016, **388**, 2873–2884.
64 Y. Soeda, M. Saito, S. Maeda, K. Ishida, A. Nakamura, S. Kojima and A. Takashima, *J. Alzheimers Dis.*, 2019, **68**, 1677–1686.
65 Y. Huang, J. Wen, L.-M. Ramirez, E. Gümüşdil, P. Pokhrel, V. H. Man, H. Ye, Y. Han, Y. Liu, P. Li, Z. Su, J. Wang, H. Mao, M. Zweckstetter, S. Perrett, S. Wu and M. Gao, *Nat. Commun.*, 2023, **14**, 5444.
66 H.-L. Zhu, C. Fernández, J.-B. Fan, F. Shewmaker, J. Chen, A. P. Minton and Y. Liang, *J. Biol. Chem.*, 2010, **285**, 3592–3599.
67 Y. Fichou, Y. Lin, J. N. Rauch, M. Vigers, Z. Zeng, M. Srivastava, T. J. Keller, J. H. Freed, K. S. Kosik and S. Han, *Proc. Natl. Acad. Sci. U.S.A.*, 2018, **115**, 13234–13239.
68 W. Zhang, B. Falcon, A. G. Murzin, J. Fan, R. A. Crowther, M. Goedert and S. H. Scheres, *eLife*, 2019, **8**, e43584.
69 G. H. Patterson and J. Lippincott-Schwartz, *Science*, 2002, **297**, 1873–1877.
70 L. Bakota, R. Brandt and J. J. Heinisch, *Mol. Genet. Genomics*, 2012, **287**, 313–324.
71 M. Igaev, D. Janning, F. Sündermann, B. Niewidok, R. Brandt and W. Junge, *Biophys. J.*, 2014, **107**, 2567–2578.
72 R. Brandt, J. Léger and G. Lee, *J. Cell Biol.*, 1995, **131**, 1327–1340.
73 A. Gauthier and R. Brandt, *Biol. Chem.*, 2010, **391**, 639–643.
74 L. Pinzi, C. Conze, N. Bisi, G. D. Torre, A. Soliman, N. Monteiro-Abreu, N. I. Trushina, A. Krusenbaum, M. K. Dolouei, A. Hellwig, M. S. Christodoulou, D. Passarella, L. Bakota, G. Rastelli and R. Brandt, *Nat. Commun.*, 2024, **15**, 1679.
75 N. Tonali, J. Kaffy, J.-L. Soulier, M. L. Gelmi, E. Erba, M. Taverna, C. van Heijenoort, T. Ha-Duong and S. Ongeri, *Eur. J. Med. Chem.*, 2018, **154**, 280–293.

View Article Online
DOI: 10.1039/D6OB00187D

Data availability statements:

The data supporting this article have been included as part of the Supplementary Information. Supplementary information: Tables, NMR spectra and further experimental details.

Thierry Milcent
Université Paris-Saclay, CNRS, BioCIS
thierry.milcent@universite-paris-saclay.fr